

OPEN

Polar mesoporous zinc sulfide nanosheets encapsulated in reduced graphene oxide three-dimensional foams for sulfur host

Limin Mao, Fei Wang & Jian Mao *

Lithium-sulfur (Li-S) batteries exhibit the high specific capacity and energy density, but prevented by the low coulombic efficiency and weak cycle life. Herein, we fabricate reduced graphene oxide (r-GO) three-dimensional (3D) foams encapsulating polar mesoporous zinc sulfide (ZnS) nanosheets and subsequently utilize the ZnS/r-GO foams to load sulfur (ZnS/r-GO/S) as cathodes for improving the performance of Li-S batteries. The mesoporous diameter of the ZnS nanosheets is approximately 10–30 nm and lots of pores in the 3D foams are observed. The porous structure provides abundant sites to adsorb and accommodate sulfur species. The cathode of the ZnS/r-GO/S exhibits 1259 mA h g⁻¹ of initial capacity and 971.9 mA h g⁻¹ of the reversible capacity after 200 cycles at 0.1C (1C = 1675 mA g⁻¹). At 1C, it still exhibits the tiny capacity decay rate of 0.019% per cycle after 300 cycles. This work may be adopted to combine the nonpolar and polar materials as a 3D network structure for high-performance Li-S batteries.

Lithium-sulfur (Li-S) batteries, as the most promising next-generation rechargeable batteries, possess an ultra-high theoretical specific capacity of 1675 mA h g⁻¹ and excellent theoretical energy density of 2600 Wh Kg⁻¹, up to five times greater than commercial LIBs (387 Wh Kg⁻¹ for LiCoO₂/C battery)^{1,2}. In addition, sulfur element is abundant, low-cost and environmentally inert³. Therefore, Li-S batteries are supposed to most promising candidate energy device to satisfy the request of electronic equipment and the demand of preferable pure electric vehicles⁴. However, Li-S batteries are still impeded by the low coulombic efficiency and the poor cycling stability, due to three factors: (1) the insulation of sulfur and its final product Li₂S/Li₂S₂, (2) large volume change during charge and discharge, and (3) the shuttling effect. The insulation of sulfur and Li₂S₂/Li₂S limits the redox reaction, causing the low utilization of active materials. Consequently, uniform dispersion of sulfur and good electrical contact with conductive matrixes are essential⁵. Volume change of sulfur under alloying is approximately 80%, making the electrode broken easily⁶. Many porous materials and internal void nanoarchitectures were designed to accommodate the expansion⁷. Shuttling effect is the critical issue in Li-S batteries, which causes low charge efficiency and poor cyclic stability. Many researches manifested that physical trapping by porous nanostructure and chemical affinity by polar materials can hinder shuttling effect available^{8,9}.

Up to now, sulfur was loaded into various materials with diverse morphologies, including carbonaceous materials^{10–12}, conductive polymers^{13–15}, metal oxides^{16,17}, and metal sulfides^{18,19}, etc. Carbonaceous frameworks were popular on account of their good conductivity and abundant morphologies, such as meso/microporous²⁰, fiber-like and foam-like structure^{21,22}. Graphene with high surface area, chemical stability, mechanical strength and flexibility, was utilized as a common energy material²³. Nevertheless, the graphene is nonpolar nature, so polysulfides are easy to escape from the surface of graphene²⁴. Oxides and sulfides are better in restraining polysulfides migrating due to their polarity^{19,25}. Metal sulfides have a strong affinity for polysulfides caused by strong sulfiphilic property, but suffering from low conductivity²⁶. Therefore, studies in combination the graphene and polar materials to achieve the good conductivity and reduce polysulfides shuttling were prominent²⁷.

Herein, we designed a three-dimensional (3D) porous foams, constructed by high conductive reduced graphene oxide (r-GO), to encapsulate polar mesoporous ZnS nanosheets by a facile water bath method. Then, the ZnS/r-GO foams loaded sulfur as composite electrodes for high-performance Li-S batteries. The r-GO foam and ZnS nanosheets were used to load sulfur as contrasted. The schematic illustration was shown in Fig. 1. The

College of Materials Science and Engineering, Sichuan University, Chengdu, 610065, China. *email: maojian@scu.edu.cn

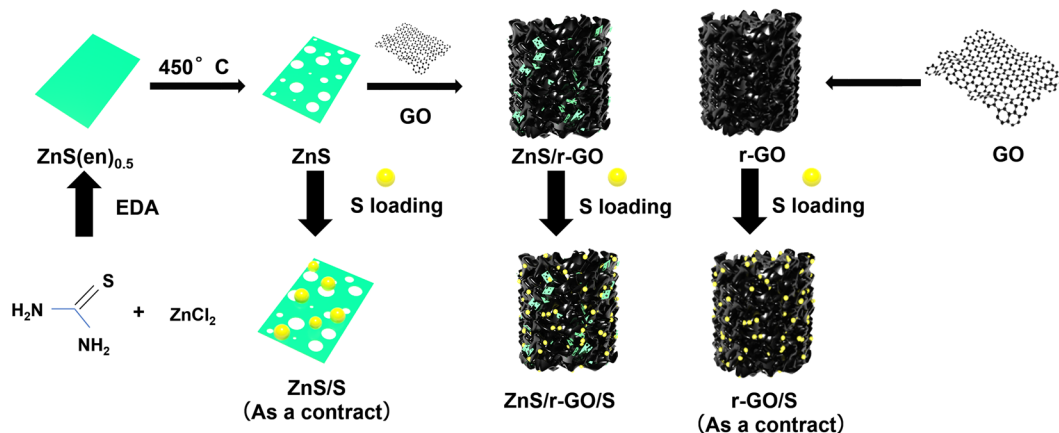


Figure 1. Schematic illustration showing the preparation ZnS/S, r-GO/S and ZnS/r-GO/S foams composites.

mesoporous ZnS nanosheets were synthesized by sintering zinc sulfide ($C_2H_4(NH_2)_2$)_{0.5} ($ZnS(en)_{0.5}$) precursor with a superior catalysis^{28,29}. The strong interaction with soluble polysulfides and catalytic activation of ZnS makes sure the sulfur utilization and stable cycle performance^{30,31}. The 3D porous r-GO network possessed high conductivity, promoting the rapid diffusion of Li^+ , but also providing the abundant sites to accommodate the sulfur species and release the expansion. The cathode of the 3D ZnS/r-GO/S foams represented excellent electrochemical performance, such as the high initial capacity of 1259 mA h g^{-1} and a stable capacity retention of $971.9 \text{ mA h g}^{-1}$ after 200 cycles at 0.1C ($1C = 1675 \text{ mA g}^{-1}$), remarkable coulombic efficiency of close to 100% as well as low capacity fading rate of 0.019% per cycle after 300 cycles at 1C.

Results and Discussion

The SEM and TEM, HR-TEM images were shown in Fig. 2. The $ZnS(en)_{0.5}$ was composed of large quantities of smooth nanosheets with the thickness of 60~100 nm, and the large range of a few to a dozen micrometers in lateral dimensions (Fig. 2a). The mesoporous ZnS succeeded to the similar sheet nanostructure in Fig. 2b, and the porosities were triggered by the decomposition of ethylenediamine (EDA)³², which could provide more sites to adsorb and catalyze polysulfides. The insert TEM image showed that the pore diameter was approximately 10~30 nm. HRTEM observation in Fig. 2c showed well-resolved lattice planes with a lattice spacing of 0.33 nm (Corresponding to (100) plane of ZnS). The SEM of the ZnS/r-GO foams (Fig. 2d) indicated that the ZnS nanosheets were encapsulated in the r-GO foams. The insert was the cross section SEM of ZnS/r-GO, manifested the 3D porous structure of the prepared composite, which played a vital role in accommodating sulfur and confinement physically to polysulfides. The loaded sulfur was distributed in the ZnS/r-GO composite as Fig. 2e. The EDS mapping (Fig. 2f) of Zn and S elements elucidated the uniform distribution of sulfur and the ZnS nanosheets.

The XRD patterns of these samples were shown in Fig. 3a. The $ZnS(en)_{0.5}$ was indexed in the orthorhombic system, consistent with the previous studies^{29,33}. After 450 °C annealing, the EDA was decomposed and the product was transformed to wurtzite ZnS ³⁴. Compared with the XRD pattern of the r-GO, the ZnS/r-GO composite had no obvious peak at approximate 26° , corresponding to (002) plane of r-GO. It probably resulted from the ZnS nanosheets preventing the restocking of the r-GO nanosheets³⁵. The sulfur of the ZnS/r-GO/S was indexed to the orthorhombic system (JCPDS card 08-0247).

The thermogravimetry (TG) curves of the ZnS/r-GO/S composite and r-GO in N_2 atmosphere were shown in Fig. 3b. The plummet of the ZnS/r-GO/S composite mainly due to the evaporation of the sulfur. The curve of the r-GO presented near-linear decline, which may cause by the decomposed of the unreduced oxygen functional group. Compared with the curve of the r-GO, the decline of the ZnS/r-GO/S composite was comprised of 11% and 61% resulted from the r-GO and sulfur, respectively. After heated to over 300 °C, the almost parallel curves also indicated that the declined weight of the ZnS/r-GO/S composite influenced by the r-GO.

X-ray photoelectron spectroscopy (XPS) was conducted to further investigate the chemical states of the ZnS/r-GO foams in Fig. 4. The wide spectra (Fig. 4a) showed the presence of C 1s, O 1s, Zn 2p and S 2p peaks. The C 1s spectrum (Fig. 4b) exhibited a noteworthy peak at 284.5 eV, ascribed to C-C/C=C. Other peaks located at 285.9 and 289.3 eV were ascribed to C-O/C-O-C and O=C-O/C=O, respectively. Figure 4c,d showed the S 2p and Zn 2p spectra of ZnS/r-GO composite and ZnS nanosheets. The peak separation of the peaks at 1022.5 and 1045.9 eV in Zn 2p spectrum of ZnS/r-GO composite was 23.0 eV, which was originated from the Zn 2p_{3/2} and Zn 2p_{1/2} of ZnS³⁶. Compared with the ZnS nanosheets, there was a positive shift of 1.05 and 0.98 eV for Zn 2p_{3/2} and Zn 2p_{1/2} of ZnS/r-GO composite, respectively. Correspondingly, the S 2p could be deconvoluted into the peaks at 162.0 and 162.9 eV, assigned to S 2p_{3/2} and S 2p_{1/2} of ZnS. The peaks in S 2p spectrum of ZnS/r-GO composite also shifted to the higher binding energy. These indicated the electronically coupled between ZnS and r-GO³⁷.

The electrochemical performance of ZnS/r-GO/S and ZnS/S cathodes was displayed in Fig. 5. The cycle performance of ZnS/r-GO/S, r-GO/S and ZnS/S at 0.1 C were exhibited in Fig. 5a. The initial specific capacities of ZnS/r-GO/S, r-GO/S and ZnS/S were 1259.4, 1205.3 and 910.2 mA h g^{-1} , respectively, retained the reversible capacity of 1059.2, 879.0 and 626.6 mA h g^{-1} after 100 cycles. The ZnS/S cathode exhibited a lower initial specific capacity and dramatic capacity fading in the second cycle. However, between 3 and 100 cycles, the

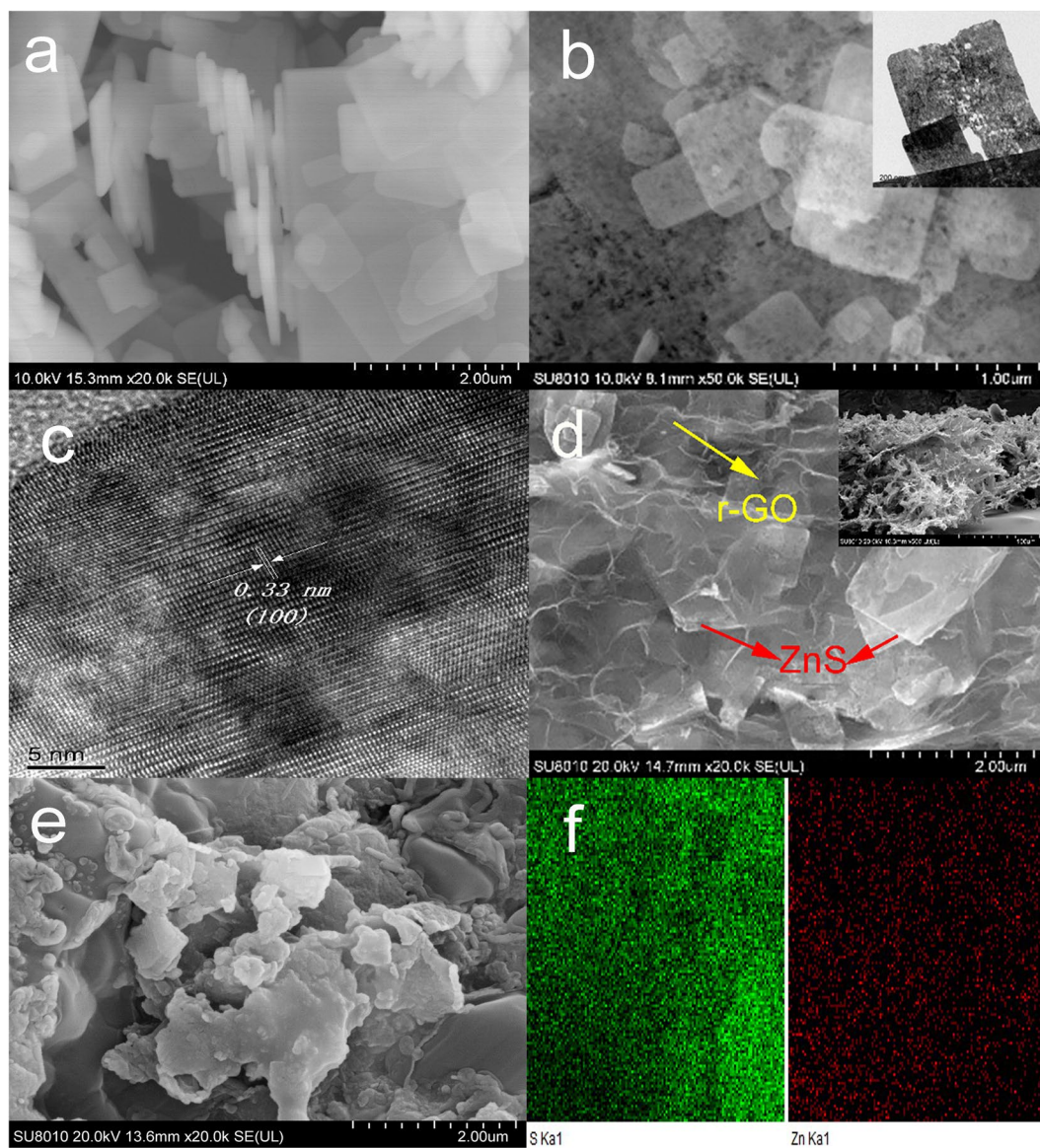


Figure 2. SEM and TEM images of the samples. (a) ZnS(en)_{0.5}, (b) mesoporous ZnS, the insert is TEM image of mesoporous ZnS. (c) HRTEM image of mesoporous ZnS, (d) SEM images of ZnS/r-GO, the insert is the cross section SEM of ZnS/r-GO. ZnS nanosheets were guided by red arrows, and r-GO was guided by yellow arrows. (e) SEM image of ZnS/r-GO/S. (f) the EDS mapping of (e).

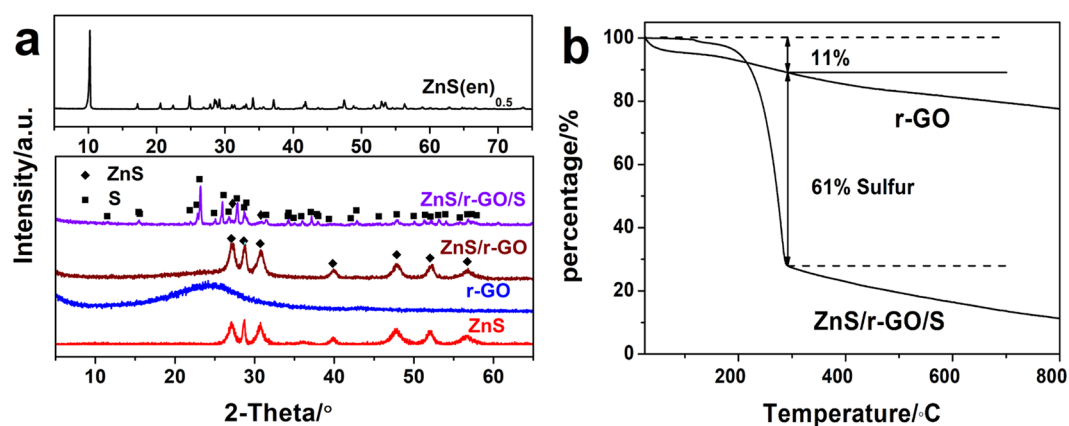


Figure 3. XRD patterns and TG curves of the samples. (a) XRD patterns of ZnS(en)_{0.5}, ZnS, r-GO, ZnS/r-GO and ZnS/r-GO/S. (b) TG curves of ZnS/r-GO/S and r-GO.

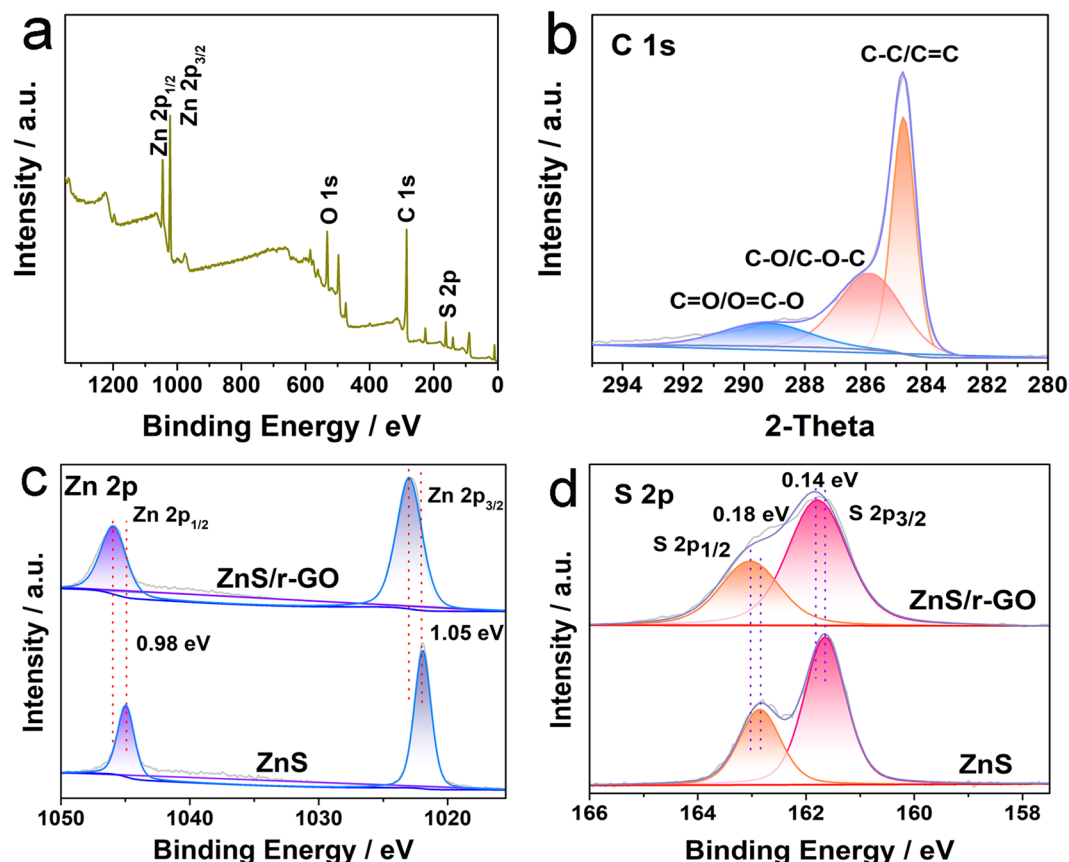


Figure 4. XPS spectra of the ZnS/r-GO and ZnS composite. (a) Wide spectrum of ZnS/r-GO. (b) C 1s spectrum of ZnS/r-GO. (c,d) S 2p and Zn 2p spectra of ZnS/r-GO composite and ZnS nanosheets.

specific capacity maintained stable, suggesting that the ZnS had a strong affinity and good catalytic activity to polysulfides. The almost coincident galvanostatic charge/discharge curves of the ZnS/S cathode at 10th, 50th and 100th (Fig. 5b) confirmed the stable cycle. Because of the high specific surface area and high conductivity of the r-GO 3D network, the ZnS/r-GO/S and r-GO/S exhibited a higher initial specific capacity. In the first few cycles, both ZnS/r-GO/S and r-GO/S showed a severe capacity fading, after that, the specific capacity increased gradually. The reasons were as follows: as the electrolyte penetrated, the sulfur loaded in the 3D foams would gradually react with Li^+ ; and for the ZnS/r-GO/S cathode, owing to the strong adsorption and catalysis of ZnS^{31,38}, the mesoporous ZnS encapsulated in 3D foams would gradually adsorb polysulfides dissolving in electrolyte and catalyze the conversion of sulfur redox³⁰. The above was also proved by the manifested second charge/discharge voltage profiles at the 50th and 100th cycle of the ZnS/r-GO/S cathode, which were longer than that at the 10th cycle with the similar first voltage profiles (Fig. 5c). The 50th and 100th cycle displayed specific capacities of 607.9 and 597.6 mA h g^{-1} at the second plateau, nonetheless the second plateau of the 10th only discharged 323.9 mA h g^{-1} . The synergistic effect of the high conductive 3D network and strong-sulfiphilic ZnS made the ZnS/r-GO/S cathode deliver more excellent electrochemical performance. Even after 200 cycles, the reversible capacity of the ZnS/r-GO/S was 971.9 mA h g^{-1} .

CV curves of the ZnS/r-GO/S were recorded at a scan rate of 0.1 mV s^{-1} in the potential range of 1.7–2.7 V (vs. Li/Li^+). The typical redox reaction of sulfur cathodes was presented in Fig. 5d. In the first cycle, two reduction peaks at 2.29 V and 2.02 V were observed, ascribing to the formation of long-chain lithium polysulfides and the further reduction to the short-chain lithium sulfides, respectively. In the third cycle, the reduction peak at 2.29 V shifted to higher potential (2.32 V). It demonstrated faster electrochemical kinetics and lower cell polarization, meaning the better cycle reversibility of the ZnS/r-GO/S cathode¹¹.

The long-term cycling performance of the ZnS/r-GO/S at 1 C after activation in first three cycles at 0.1 C was shown in Fig. 6a. After 300 cycles, a discharge specific capacity of 646.3 mA h g^{-1} with ~100% coulombic efficiency was remained, corresponding to a low capacity fading of 0.019% per cycle. The rate capacity (Fig. 6b) of the ZnS/r-GO/S was measured at different current rate in the potential range of 1.7–2.7 V (vs. Li/Li^+). When the rate turned back to 0.1 C after each 10 cycles at 0.1 C, 0.2 C, 0.5 C and 1 C, a discharge capacity of approximately 800 mA h g^{-1} was recovered, indicating the stable rate performance.

The Li_2S_6 adsorption was measured to visually observe the affinity of the ZnS/r-GO, r-GO and ZnS to polysulfides, and the UV-vis spectra were carried out to test the concentration of Li_2S_6 solutions (Shown in Fig. 6c). In the inset photograph, the noticeable fade in color of the Li_2S_6 solutions was observed after adding the ZnS/r-GO and r-GO due to the disproportionation of the polysulfides³⁹ and the adsorption of samples. The affinity of r-GO

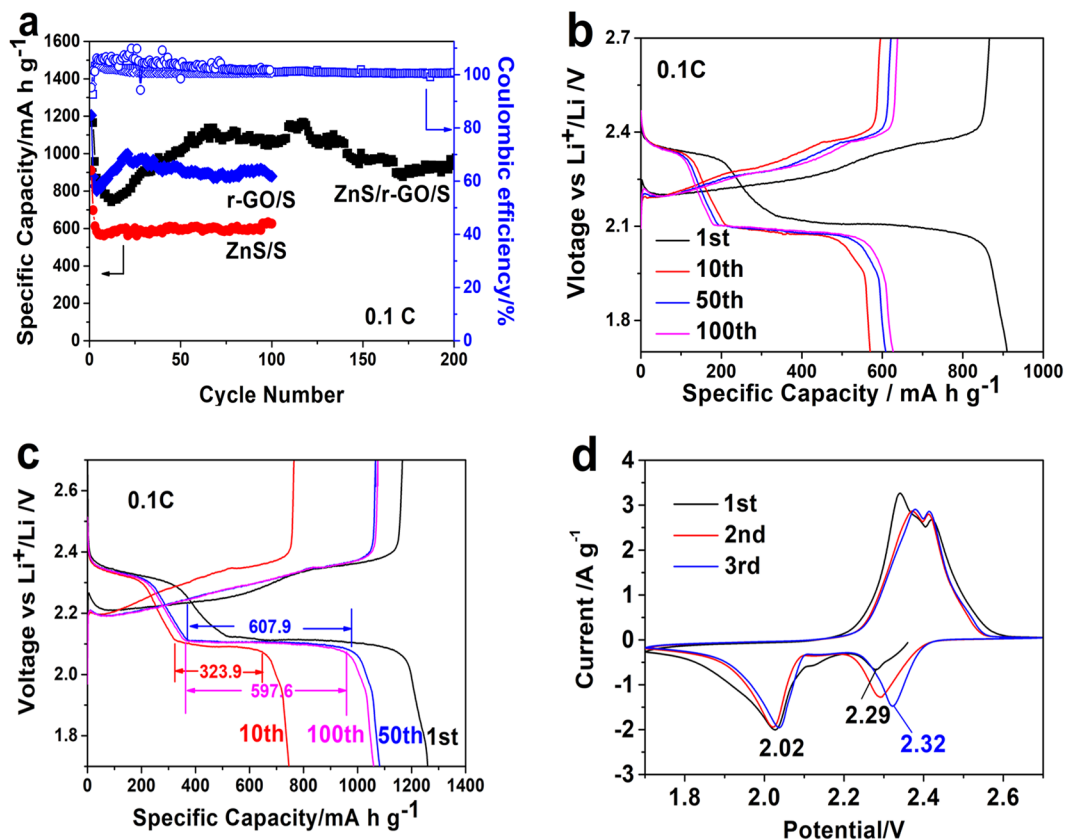


Figure 5. Electrochemical performance of ZnS/r-GO/S, r-GO/S and ZnS/S electrodes. (a) Cycle performance at 0.1 C of ZnS/r-GO/S, r-GO/S and ZnS/S electrodes, respectively. (b,c) Galvanostatic charge/discharge profiles of ZnS/S and ZnS/r-GO/S cathode at 0.1 C. (d) CV curves of ZnS/r-GO/S electrode.

to polysulfides may be caused by the higher specific area. On the other hand, the change in color of the Li₂S₆ solution of ZnS treatment was lighter. In the UV-vis spectra, a strong absorbance was observed at 420 and 465 nm in fresh Li₂S₆ solution, which ascribed to the adsorption peaks of the Li₂S₆. The absorbance of ZnS was declined slightly, and the peaks were still visible. For the solutions after the r-GO and ZnS/r-GO treatment, the peak almost disappeared, indicating that the r-GO and ZnS/r-GO foams had strong affinity to Li₂S₆. From the UV spectra, the ZnS/r-GO foams combining the polarity of ZnS and the high specific surface area of r-GO exhibited the best absorptivity to the Li₂S₆.

In summary, the 3D foams comprised by polar mesoporous ZnS nanosheets and r-GO was fabricated, then the sulfur was loaded into the foams as the Li-S batteries cathodes. The pore diameter of the mesoporous ZnS nanosheets was 10–30 nm and the ZnS/r-GO composite possessed lots of pores. The 3D ZnS/r-GO foams loaded sulfur exhibited excellent electrochemical properties, initial specific capacity of 1259 mA h g⁻¹ and a reversible capacity of 971.9 mA h g⁻¹ after 200 cycles at 0.1 C, due to the polar adsorption to polysulfides by the mesoporous ZnS and the excellent Li⁺ or electrons diffusion of the r-GO foams. This work may provide a way to combine the nonpolar and polar materials as a 3D network structure for high-performance Li-S batteries.

Methods

Preparation of the ZnS(en)_{0.5}, mesoporous ZnS nanosheets, r-GO and ZnS/r-GO 3D foams. EDA as solvent, the mesoporous ZnS nanosheets were synthesized by solvothermal and subsequent calcination²⁸. 2 mmol ZnCl₂ and 4 mmol CS(NH₂)₂ were mixed uniformly, then dissolved in 60 ml EDA with ultrasonic for 30 min. The solution was quickly poured into 100 mL autoclave, solvothermal at 180 °C for 12 h. After centrifuging and cleaning, drying at 60 °C for hours, the ZnS(en)_{0.5} precursor was obtained. The mesoporous ZnS nanosheets were got by calcinating the ZnS(en)_{0.5} at 450 °C for 30 min in air. The ZnS/r-GO 3D foams were synthesized by a facile excess ascorbic acid reduction method and the mass ratio of the ZnS and GO was 1:1. The mixture in distilled water was sonicated for 10 min, and then heated at 90 °C for 2 h in a water bath. The freeze drying was used to keep the porous structure. The r-GO foam was prepared by the same method of ZnS/r-GO for a contract.

Preparation of the ZnS/S, r-GO/S and ZnS/r-GO/S composites. The ZnS/S, r-GO/S and ZnS/r-GO/S composites were prepared by the conventional melt-diffusion method. Typically, sulfur powders and the samples (ZnS, r-GO or ZnS/r-GO) in a mass ratio of 3:2 were homogenized by ground in an agate mortar. The mixtures were sealed in 25 mL Teflon-lined stainless-steel autoclave with argon in glove box, maintained at 155 °C for 12 h.

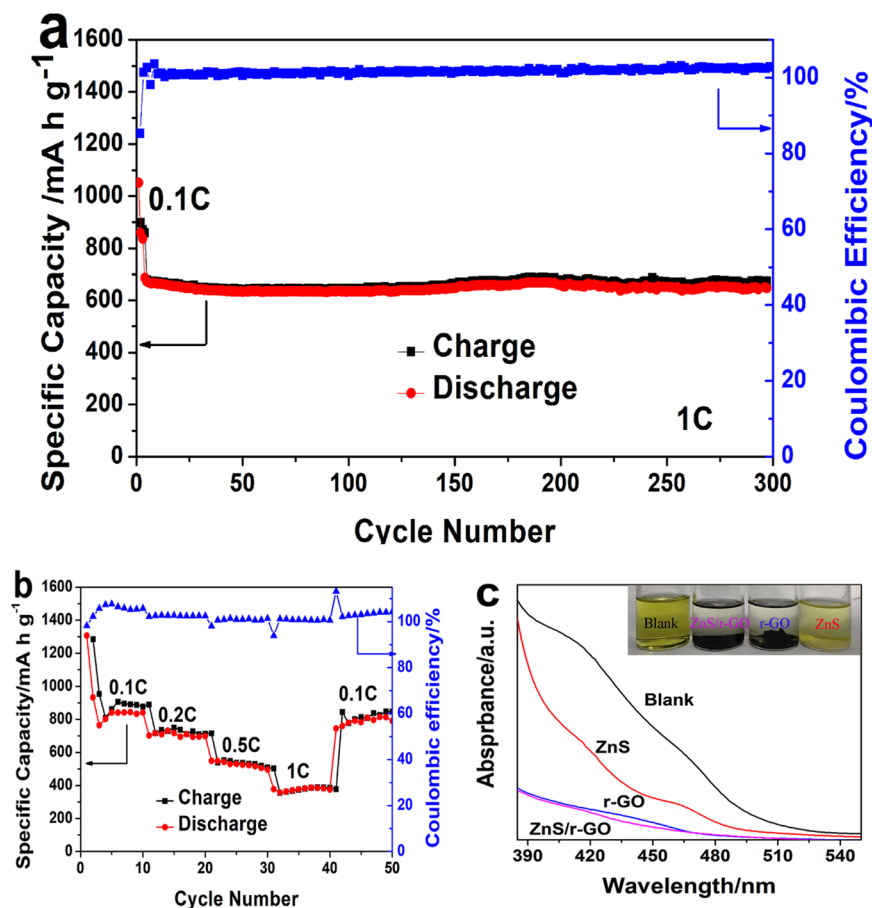


Figure 6. Electrochemical performance and Polysulfides adsorption. (a) Long-term cycling performance of ZnS/r-GO/S at 1 C after activation in first three cycles at 0.1 C. (b) Rate capacity of ZnS/r-GO/S, (c) UV-vis spectra of the Li₂S₆ solution with blank, ZnS, r-GO and ZnS/r-GO. (Inset photograph of visualized adsorption of Li₂S₆ on ZnS, r-GO and ZnS/r-GO with same mass).

Characterization. SEM images were obtained with a scanning electron microscope. TEM and high-resolution TEM (HRTEM) images were performed by a transmission electron microscopy at 200 KV. The X-ray diffraction measurements were carried out using an X-ray powder diffractometer, performed in transmission geometry with Cu K_{α1} radiation ($\lambda = 1.5418 \text{ \AA}$). The samples were measured at the sweep rate of 5° min^{-1} . X-ray photoelectron spectroscopy (XPS) measurements were performed on a Kratos XSAM 800 (UK). UV-vis spectra of the Li₂S₆ solutions exposed to different adsorbents were collected on a UV-vis spectrometer. The sulfur contents of composites were determined using thermo-gravimetry analyses (TGA) on a DTG-60 from the room temperature to 800°C with a heating rate of $10^\circ \text{C min}^{-1}$ in Ar.

Polysulfides adsorption tests. Lithium polysulfide (Li₂S₆) solution was prepared as the literature reported¹⁹. The stoichiometric ratio amounts of sublimed sulfur and lithium sulfide (Li₂S) with a molar ratio of 5:1 were dissolved in 1:1 (v/v) DOL/DME, then sealed in an argon-filled glove box, stirred at 60°C for 48 h in the ambient environment. 10 mg the ZnS, r-GO or ZnS/r-GO was added in an 8 mL Li₂S₆ solution (1 mmol L^{-1}) and stewed for 24 h. The UV-vis spectra were tested to analyze the adsorption ability of the ZnS, r-GO or ZnS/r-GO for Li₂S₆.

Cell assembly and electrochemical measurements. The electrochemical tests were performed using a coin type 2032 half-cell with lithium metal (purity 99.95%, 0.6 mm thick and 15.8 mm in diameter) as counter and reference electrodes, and the polypropylene films (Ceglard 2400) were as separators. The electrode slurry was composed of 80 wt. % active materials (the ZnS/S, r-GO/S or ZnS/r-GO/S), 10 wt. % acetylene black and 10 wt. % polyvinylidene fluoride (PVDF), moderate n-methyl-2-pyrrolidinone (NMP) as solvent. The active materials and acetylene black, PVDF were ground uniformly in an agate mortar for 1 h. The slurry was coated onto carbon paper (thickness of $20 \mu\text{m}$) with subsequent heating at 60°C for 24 h in vacuum. The composite carbon paper was then punched into disk with 14.2 mm in diameter to be used as cathodes. The areal sulfur loadings were ranged at $1.3 \sim 2.2 \text{ mg cm}^{-2}$. 1 mol L^{-1} lithium bistrifluoromethyl sulfimide (LiTFSI) in DME and DOL (1:1 v/v) with 2 wt. % LiNO₃ was used as the electrolyte. The galvanostatic charge/discharge performance of the cells was tested on a multichannel battery tester (LANDCT) in the potential range of 1.7~2.7 V vs. Li⁺/Li electrodes at room temperature. Cyclic Voltammetry (CV) measurements were performed at a scan rate of 0.1 mV s^{-1} on an electrochemical workstation. Applied currents and specific capacities were calculated on the basis of the mass ratio of S in the cathodes.

Received: 11 October 2019; Accepted: 6 March 2020;

Published online: 24 March 2020

References

- Manthiram, A., Fu, Y. & Su, Y.-S. Challenges and prospects of lithium sulfur batteries. *Acc. Chem. Res.* **46**, 1125–1134 (2013).
- Yin, Y. X., Xin, S., Guo, Y. G. & Wan, L. J. Lithium-sulfur batteries: electrochemistry, materials, and prospects. *Angew. Chem. Int. Ed. Engl.* **52**, 13186–13200, <https://doi.org/10.1002/anie.201304762> (2013).
- Bu, Y. *et al.* Sandwich-type porous carbon/sulfur/polyaniline composite as cathode material for high-performance lithium-sulfur batteries. *RSC Adv.* **6**, 104591–104596, <https://doi.org/10.1039/c6ra23943a> (2016).
- Xiang, K., Cai, S., Wang, X., Chen, M. & Jiang, S. Nitrogen-doped activated microporous carbon spheres as a sulfur matrix for advanced lithium-sulfur batteries. *J. Alloy. Compd.* **740**, 687–694, <https://doi.org/10.1016/j.jallcom.2018.01.026> (2018).
- Pope, M. A. & Aksay, I. A. Structural design of cathodes for Li-S batteries. *Adv. Energy Mater.* **5**, 1500124, <https://doi.org/10.1002/aenm.201500124> (2015).
- Manthiram, A., Fu, Y., Chung, S. H., Zu, C. & Su, Y. S. Rechargeable lithium-sulfur batteries. *Chem. Rev.* **114**, 11751–11787, <https://doi.org/10.1021/cr500062v> (2014).
- Li, X., Wang, Y., Xu, C. & Pan, L. Mesoporous carbon/sulfur composite with N-doping and tunable pore size for high-performance Li-S batteries. *J. Solid. State Electrochem.* **21**, 1101–1109, <https://doi.org/10.1007/s10008-016-3453-7> (2016).
- Wei, H. *et al.* Chemical bonding and physical trapping of sulfur in mesoporous Magnéli Ti₄O₇ microspheres for high-performance Li-S battery. *Adv. Energy Mater.* **7**, 1601616, <https://doi.org/10.1002/aenm.201601616> (2017).
- He, J., Luo, L., Chen, Y. & Manthiram, A. Yolk-shelled C@Fe₃O₄ nanoboxes as efficient sulfur hosts for high-performance lithium-sulfur batteries. *Adv. Mater.* **29**, <https://doi.org/10.1002/adma.201702707> (2017).
- Chen, S. R. *et al.* Ordered mesoporous carbon/sulfur nanocomposite of high performances as cathode for lithium-sulfur battery. *Electrochim. Acta* **56**, 9549 (2011).
- Zhao, Q. *et al.* A 3D conductive carbon interlayer with ultrahigh adsorption capability for lithium-sulfur batteries. *Appl. Surf. Sci.* **440**, 770–777, <https://doi.org/10.1016/j.apsusc.2018.01.162> (2018).
- Chen, R. *et al.* Graphene-based three-dimensional hierarchical sandwich-type architecture for high-performance Li/S batteries. *Nano Lett.* **13**, 4642–4649, <https://doi.org/10.1021/nl4016683> (2013).
- Zhang, Y. *et al.* The construction of high sulfur content spherical sulfur-carbon nanotube-polyethylene glycol-nickel nitrate hydroxide composites for lithium sulfur battery. *J. Alloy. Compd.* **729**, 331–337, <https://doi.org/10.1016/j.jallcom.2017.09.131> (2017).
- Yin, L., Wang, J., Yang, J. & Nuli, Y. A novel pyrolyzed polyacrylonitrile-sulfur@MWCNT composite cathode material for high-rate rechargeable lithium/sulfur batteries. *J. Mater. Chem.* **21**, 6807 (2011).
- Li, H. *et al.* Three-dimensionally ordered hierarchically porous polypyrrole loading sulfur as high-performance cathode for lithium/sulfur batteries. *Polym.* **137**, 261–268, <https://doi.org/10.1016/j.polymer.2018.01.022> (2018).
- Wei Seh, Z. *et al.* Sulphur-TiO₂ yolk-shell nanoarchitecture with internal void space for long-cycle lithium-sulphur batteries. *Nat. Commun.* **4**, 1331, <https://doi.org/10.1038/ncomms2327> (2013).
- Demir-Cakan, R. *et al.* Cathode composites for Li-S batteries via the use of oxygenated porous architectures. *J. Am. Chem. Soc.* **133**, 16154 (2011).
- Cha, E. *et al.* 2D MoS₂ as an efficient protective layer for lithium metal anodes in high-performance Li-S batteries. *Nat. Nanotechnol.* **13**, 337–344, <https://doi.org/10.1038/s41565-018-0061-y> (2018).
- Lei, T. *et al.* Multi-functional layered WS₂ nanosheets for enhancing the performance of lithium-sulfur batteries. *Adv. Energy Mater.* **7**, 1601843, <https://doi.org/10.1002/aenm.201601843> (2017).
- Zhang, L. *et al.* High-content of sulfur uniformly embedded in mesoporous carbon: a new electrodeposition synthesis and an outstanding lithium-sulfur battery cathode. *J. Mater. Chem. A* **5**, 5905–5911, <https://doi.org/10.1039/c7ta00328e> (2017).
- Zhang, X.-Q., He, B., Li, W.-C. & Lu, A.-H. Hollow carbon nanofibers with dynamic adjustable pore sizes and closed ends as hosts for high-rate lithium-sulfur battery cathodes. *Nano Res.* **11**, 1238–1246, <https://doi.org/10.1007/s12274-017-1737-6> (2018).
- Zhang, Y., Sun, L., Li, H., Tan, T. & Li, J. Porous three-dimensional reduced graphene oxide for high-performance lithium-sulfur batteries. *J. Alloy. Compd.* **739**, 290–297, <https://doi.org/10.1016/j.jallcom.2017.12.294> (2018).
- Wang, F., Wang, H. & Mao, J. Aligned-graphene composites: a review. *J. Mater. Sci.* **54**, 36–61, <https://doi.org/10.1007/s10853-018-2849-4> (2019).
- Tao, X. *et al.* Balancing surface adsorption and diffusion of lithium-polysulfides on nonconductive oxides for lithium-sulfur battery design. *Nat. Commun.* **7**, <https://doi.org/10.1038/ncomms11203> (2016).
- Liang, X. & Nazar, L. F. In situ reactive assembly of scalable core-shell sulfur-MnO₂ composite cathodes. *ACS Nano* **10**, 4192–4198, <https://doi.org/10.1021/acsnano.5b07458> (2016).
- Liu, X., Huang, J. Q., Zhang, Q. & Mai, L. Nanostructured metal oxides and sulfides for lithium-sulfur batteries. *Adv. Mater.* **29**, <https://doi.org/10.1002/adma.201601759> (2017).
- Gao, C. *et al.* Rational design of multi-functional CoS@rGO composite for performance enhanced Li-S cathode. *J. Power Sources* **421**, 132–138, <https://doi.org/10.1016/j.jpowsour.2019.03.015> (2019).
- Yu, S. H. & Yoshimura, M. Shape and phase control of ZnS nanocrystals: Template fabrication of wurtzite ZnS single-crystal nanosheets and ZnO flake-like dendrites from a lamellar molecular precursor ZnS-(NH₂CH₂CH₂NH₂)(0.5). *Adv. Mater.* **14**, 296–+, doi:10.1002/1521-4095(20020219)14:4<296::aid-adma296>3.3.co;2-y (2002).
- Ni, Y. H. *et al.* Preparation, conversion, and comparison of the photocatalytic and electrochemical properties of ZnS(en)(0.5), ZnS, and ZnO. *Cryst. Growth Des.* **7**, 280–285, <https://doi.org/10.1021/cg060312z> (2007).
- Xu, J. *et al.* Promoting lithium polysulfide/sulfide redox kinetics by the catalyzing of zinc sulfide for high performance lithium-sulfur battery. *Nano Energy* **51**, 73–82, <https://doi.org/10.1016/j.nanoen.2018.06.046> (2018).
- Chen Long, L. J.-D. & Zhang S.-Q. Preparation of mesoporous carbon/sulfur composite loaded with ZnS and its property for lithium-sulfur batteries. *J. Inorg. Mater.*, **1127** (2017).
- Liu, J. *et al.* Novel porous single-crystalline ZnO nanosheets fabricated by annealing ZnS(en)_{0.5} (en = ethylenediamine) precursor. Application in a gas sensor for indoor air contaminant detection. *Nanotechnol.* **20**, 125501, <https://doi.org/10.1088/0957-4484/20/12/125501> (2009).
- Ouyang, X. *et al.* Ab initio structure study from in-house powder diffraction of a novel ZnS(EN)_{0.5} structure with layered wurtzite ZnS fragment. *Chem. Comm.*, 886–887, <https://doi.org/10.1039/b212335p> (2003).
- Jang, J. *et al.* Topotactic synthesis of mesoporous ZnS and ZnO nanoplates and their photocatalytic activity. *J. Catal.* **254**, 144–155, <https://doi.org/10.1016/j.jcat.2007.12.010> (2008).
- Xu, C., Wang, X. & Zhu, J. W. Graphene-metal particle nanocomposites. *J. Phys. Chem. C* **112**, 19841–19845, <https://doi.org/10.1021/jp807989b> (2008).
- Golsheikh, A. M., Lim, H. N., Zakaria, R. & Huang, N. M. Sonochemical synthesis of reduced graphene oxide uniformly decorated with hierarchical ZnS nanospheres and its enhanced photocatalytic activities. *RSC Adv.* **5**, 12726–12735, <https://doi.org/10.1039/c4ra14775h> (2015).

37. Chu, K., Liu, Y. P., Li, Y. B., Wang, J. & Zhang, H. Electronically coupled SnO₂ quantum dots and graphene for efficient nitrogen reduction reaction. *ACS Appl. Mater. Interfaces* **11**, 31806–31815, <https://doi.org/10.1021/acsami.9b08055> (2019).
38. Razaq, R. *et al.* Ultrahigh sulfur loading in ZnS_{1-x}/rGO through in situ oxidation-refilling route for high-performance Li S batteries. *J. Power Sources* **414**, 453–459, <https://doi.org/10.1016/j.jpowsour.2019.01.038> (2019).
39. Liu, J., Chen, H., Chen, W., Zhang, Y. & Zheng, Y. New insight into the “shuttle mechanism” of rechargeable lithium-sulfur batteries. *ChemElectroChem* **6**, 2782–2787, <https://doi.org/10.1002/celec.201900420> (2019).

Acknowledgements

The work was supported by the Sichuan Science and Technology Program (2018GZ0459 and 2017GZ0108).

Author contributions

Jian Mao designed the research. Limin Mao conducted the experiments and deal with the results and discussions with Fei Wang. Limin Mao wrote the draft of the manuscript.

Competing interests

The authors declare no competing interests.

Additional information

Correspondence and requests for materials should be addressed to J.M.

Reprints and permissions information is available at www.nature.com/reprints.

Publisher's note Springer Nature remains neutral with regard to jurisdictional claims in published maps and institutional affiliations.



Open Access This article is licensed under a Creative Commons Attribution 4.0 International License, which permits use, sharing, adaptation, distribution and reproduction in any medium or format, as long as you give appropriate credit to the original author(s) and the source, provide a link to the Creative Commons license, and indicate if changes were made. The images or other third party material in this article are included in the article's Creative Commons license, unless indicated otherwise in a credit line to the material. If material is not included in the article's Creative Commons license and your intended use is not permitted by statutory regulation or exceeds the permitted use, you will need to obtain permission directly from the copyright holder. To view a copy of this license, visit <http://creativecommons.org/licenses/by/4.0/>.

© The Author(s) 2020